Large-Pore Mesoporous Covalent Organic Frameworks Fast Ion Sieves by Kinetics-Mediated Micelle Assembly for Aqueous Batteries

Ying Wan,[a,b,c] Lei Huang,[a,b] Fanxing Bu,*[b] Zhihao Sun,[c] Siyuan Zhang,[a] Zaiwang Zhao,[c] Laiquan Li,[d] Dongliang Chao,*[c] Dongyuan Zhao,*[c] and Wei Luo*[a]

[a] State Key Laboratory of Advanced Fiber Materials, College of Materials Science and Engineering, Donghua University, Shanghai 201620, China.
E-mail: wluo@dhu.edu.cn

[b] Institute of Cultural Heritage Science and Technology, Key Laboratory of Silicate Cultural Relics Conservation, Ministry of Education, Institute for the Conservation of Cultural Heritage, School of Cultural Heritage and Information Management, Shanghai University, Shanghai 200444, P. R. China.
E-mail: fxbu@shu.edu.cn

[c] Laboratory of Advanced Materials, Shanghai Key Laboratory of Molecular Catalysis and Innovative Materials, School of Chemistry and Materials, Fudan University, Shanghai 200433, P. R. China.
E-mail: chaod@fudan.edu.cn, dyzhao@fudan.edu.cn

[d] Institute of Energy Materials Science, University of Shanghai Science and Technology, Shanghai 200093, China.

1. Supplementary Methods

Chemicals:

1,3,5-benzenetricarboxaldehyde (BTCA), 1,4-dioxane (DIO), trimethyltriazine (TMT), and 1,3,5-tris(4-aminophenyl)benzene (TAPB) were obtained from Titan. 1,4-terephthalaldehyde (PDA), 1,3,5-trimethylbenzene (TMB), 2-bromoisobutyryl bromide, N,N,N′,N′,N′-pentamethyldiethylenetriamine (PMDETA), and p-phenylenediamine (PD) were obtained from Aladdin Reagent. Tetrahydrofuran (THF, ≥99%), pyridine (≥99%), and cuprous bromide (CuBr) were obtained from Mclean Reagent. Poly(ethylene oxide) (PEO-5000) was purchased from Sigma-Aldrich. Hydrazine hydrate (HZ) was obtained from Shushi. Cellulose nanofiber (CMC) was purchased from Tianjin Mujingling. Technology. Zinc sulfate heptahydrate ($ZnSO_4$•$7H_2O$) was purchased from Aladdin. All chemicals were used as received unless otherwise noted.

Characterizations and measurements:

Transmission electron microscopy (TEM) images were acquired on a JEOL 2100F microscope (Japan) operated at a voltage of 200 kV. Field-emission scanning electron microscopy (FE-SEM) images were obtained on a Hitachi model S-8230 field emission scanning microscope. The dynamic light scattering (DLS) and zeta potentials were measured by using a 90 Plus PALS. X-ray diffraction (XRD) patterns were recorded on a Bruker D8 powder X-ray diffractometer (Germany) with Ni-filtered Cu Kα radiation (40 kV, 40 mA). FT-IR spectra were collected by a Nicolet 7000-C spectrometer using the KBr disc method. Fluorescence curves were recorded with a F-7000 spectro-fluorophotometer. Ultraviolet-visible (UV-Vis) absorption spectra were recorded in solution using a UV-1900i spectrometer. Nitrogen sorption isotherms were tested at 77K with an Autosorb IQ analyser. Before measurement, the samples should be degassed under vacuum at 120 °C for at least 12 hours. The specific surface area was calculated using the Brunauer–Emmett–Teller (BET) method. The pore size distribution was derived from N_2 adsorption isotherms using the quenched solid density functional theory (QSDFT) model for micropores and the Barrett–Joyner–Halenda (BJH) model for mesopores.

Synthesis of diblock copolymer poly(ethylene oxide)-block-polystyrene: (PEO-PS)

The diblock copolymer was prepared by atom transfer radical polymerization (ATRP) method involving two steps. The typical synthesis process was carried out as follows.

The first step was the synthesis of macroinitiator PEO-Br. 40.0 g of monomethoxy PEO-5000 was dissolved in 240 mL of THF, then, 40 mL of pyridine was added to form a homogeneous solution at 30 °C. The solution was cooled in ice-water bath. Then, 12.00 g of 2-bromoisobutyryl bromide was added dropwise under stirring for 30 min. The resultant solution was further stirred at 30 °C for 24 h. After cooling down to room temperature, 600 mL of cold ether was added to the solution. The white product of PEO-Br was precipitated from the reaction solution. It was washed with cold ether and further dried in vacuum at 30 °C overnight. In the second step, 10.00 g of previously prepared PEO-Br, 0.30 g of CuBr, 1.00 g of PMDETA and 70 mL of styrene were added to an ampoules bottle, which was degassed with three freeze-pump-thaw cycles and sealed under vacuum. It was subsequently placed in an oil bath at 115 °C under stirring to allow polymerization of styrene. The reaction continued for 2 h, then, the system was cooled down to room temperature. The product was dissolved in 200 mL of THF and filtered through Al_2O_3 column to remove Cu complex. Petroleum ether (600 mL) was poured into the solution to precipitate PEO-PS block copolymer. The copolymer was then dried in vacuum.

Synthesis of solid BTCA-PD-COF:

20 mg of BTCA (0.123 mmol), 20 mg of PD (0.185 mmol) and 180 mg of PEO-PS were dissolved in 5.7 mL DIO. 0.3 mL water was added to trigger the reaction. The mixture was stirred at 600 rpm for 12 h at room temperature. The resultant solid BTCA-PD-COF precursor was collected by centrifugation and washed with THF three times. Then the dry solid BTCA-PD-COF precursor powder was dispersed in DIO/TMB (20 mL, 1/1 in vol) and 0.1 mL aqueous acetic acid (6 M) with sonication for 15 min. Then, the resulted solution was transferred to a 50 mL Teflon-lined stainless-steel autoclave and heated at 120 °C in an oven for 72 h. The precipitate was collected by centrifugation, washed with ethanol and dried under vacuum at 60 °C for 12 h.

Synthesis of golf-like BTCA-PD-MesoCOF:

20 mg of BTCA (0.123 mmol), 20 mg of PD (0.185 mmol) and 180 mg of PEO-PS were dissolved in 5.25 mL DIO. 0.75 mL water was added to trigger the reaction. The mixture was stirred at 600 rpm for 12 h at room temperature. The resultant golf-like BTCA-PD-MesoCOF precursor was collected by centrifugation and washed with THF three times. Then the dry golf-like BTCA-PD-MesoCOF precursor powder was dispersed in DIO/TMB (20 mL, 1/1 in vol) and 0.1 mL aqueous acetic acid (6 M) with sonication for 15 min. Then, the resulted solution was transferred to a 50 mL Teflon-

lined stainless-steel autoclave and heated at 120 °C in an oven for 72 h. The precipitate was collected by centrifugation, washed with ethanol and dried under vacuum at 60 °C for 12 h.

Synthesis of spherical BTCA-PD-MesoCOF:

20 mg of BTCA (0.123 mmol), 20 mg of PD (0.185 mmol) and 180 mg of PEO-PS were dissolved in 4.5 mL DIO. 1.5 mL water was added to trigger the reaction. The mixture was stirred at 600 rpm for 12 h at room temperature. The resultant spherical BTCA-PD-MesoCOF precursor was collected by centrifugation and washed with THF three times. Then the dry spherical BTCA-PD-MesoCOF precursor powder was dispersed in DIO/TMB (20 mL, 1/1 in vol) and 0.1 mL aqueous acetic acid (6 M) with sonication for 15 min. Then, the resulted solution was transferred to a 50 mL Teflon-lined stainless-steel autoclave and heated at 120 °C in an oven for 72 h. The precipitate was collected by centrifugation, washed with ethanol and dried under vacuum at 60 °C for 12 h.

Synthesis of dendritic BTCA-PD-MesoCOF:

20 mg of BTCA (0.123 mmol), 20 mg of PD (0.185 mmol) and 180 mg of PEO-PS were dissolved in 3 mL DIO. 4.5 mL water was added to trigger the reaction. The mixture was stirred at 600 rpm for 12 h at room temperature. The resultant dendritic BTCA-PD-MesoCOF precursor was collected by centrifugation and washed with THF three times. Then the dry dendritic BTCA-PD-MesoCOF precursor powder was dispersed in DIO/TMB (20 mL, 1/1 in vol) and 0.1 mL aqueous acetic acid (6 M) with sonication for 15 min. Then, the resulted solution was transferred to a 50 mL Teflon-lined stainless-steel autoclave and heated at 120 °C in an oven for 72 h. The precipitate was collected by centrifugation, washed with ethanol and dried under vacuum at 60 °C for 12 h.

Synthesis of walnut-like BTCA-PD-MesoCOF:

20 mg of BTCA (0.123 mmol), 20 mg of PD (0.185 mmol) and 180 mg of PEO-PS were dissolved in 3 mL DIO. 6 mL water was added to trigger the reaction. The mixture was stirred at 600 rpm for 12 h at room temperature. The resultant walnut-like BTCA-PD-MesoCOF precursor was collected by centrifugation and washed with THF three times. Then dry walnut-like BTCA-PD-MesoCOF precursor powder was dissolved in DIO/TMB (20 mL,1/1 in vol) and 0.1 mL aqueous acetic acid (6 M) with sonication for 15 min. Then, the resulted solution was transferred to a 50 mL Teflon-lined stainless-

steel autoclave and heated at 120 °C in an oven for 72 h. The precipitate was collected by centrifugation, washed with ethanol and dried under vacuum at 60 °C for 12 h.

Synthesis of BTCA-PD-COF nanoparticles:

20 mg of BTCA (0.123 mmol), 20 mg of PD (0.185 mmol) and 180 mg of PEO-PS were dissolved in 3 mL DIO. 30 mL water was added to trigger the reaction. The mixture was stirred at 600 rpm for 2 h at room temperature. The resultant BTCA-PD-COF precursor nanoparticles was collected by centrifugation and washed with THF three times. Then dry BTCA-PD-COF precursor nanoparticles powder was dissolved in DIO/TMB (20 mL, 1/1 in vol) and 0.1 mL aqueous acetic acid (6 M) with sonication for 15 min. Then, the resulted solution was transferred to a 50 mL Teflon-lined stainless-steel autoclave and heated at 120 °C in an oven for 72 h. The precipitate was collected by centrifugation, washed with ethanol and dried under vacuum at 60 °C for 12 h.

Synthesis of spherical BTCA-PD-MesoCOFs with varied concentrations of PEO-PS:

20 mg of BTCA (0.123 mmol), 20 mg of PD (0.185 mmol) and the specified dosage of PEO-PS (60, 120 and 240 mg) were dissolved in 4.5 mL DIO. 1.5 mL water was added to trigger the reaction. The mixture was stirred at 600 rpm for 12 h at room temperature. The resultant spherical BTCA-PD-MesoCOF precursor was collected by centrifugation and washed with THF three times. Then the dry spherical BTCA-PD-MesoCOF precursor powder was dispersed in DIO/TMB (20 mL, 1/1 in vol) and 0.1 mL aqueous acetic acid (6 M) with sonication for 15 min. Then, the resulted solution was transferred to a 50 mL Teflon-lined stainless-steel autoclave and heated at 120 °C in an oven for 72 h. The precipitate was collected by centrifugation, washed with ethanol and dried under vacuum at 60 °C for 12 h.

Synthesis of spherical BTCA-PD-MesoCOFs with different stirring rates:

20 mg of BTCA (0.123 mmol), 20 mg of PD (0.185 mmol) and 180 mg of PEO-PS were dissolved in 4.5 mL DIO. 1.5 mL water was added to trigger the reaction. The mixture was stirred at a specified stirring rate (900 and 1200 rpm) for 12 h at room temperature. The resultant spherical BTCA-PD-MesoCOF precursor was collected by centrifugation and washed with THF three times. Then the dry spherical BTCA-PD-MesoCOF precursor powder was dispersed in DIO/TMB (20 mL, 1/1 in vol) and 0.1 mL aqueous acetic acid (6 M) with sonication for 15 min. Then, the resulted solution

was transferred to a 50 mL Teflon-lined stainless-steel autoclave and heated at 120 °C in an oven for 72 h. The precipitate was collected by centrifugation, washed with ethanol and dried under vacuum at 60 °C for 12 h.

Synthesis of spherical BTCA-PD-MesoCOFs at different temperatures:

20 mg of BTCA (0.123 mmol), 20 mg of PD (0.185 mmol), and 180 mg of PEO-PS were dissolved in 4.5 mL DIO. 1.5 mL water was added to trigger the reaction. The mixture was stirred at 600 rpm for 12 h at a specified temperature (60 and 90 °C). The resultant spherical BTCA-PD-MesoCOF precursor was collected by centrifugation and washed with THF three times. Then the dry spherical BTCA-PD-MesoCOF precursor powder was dispersed in DIO/TMB (20 mL, 1/1 in vol) and 0.1 mL aqueous acetic acid (6 M) with sonication for 15 min. Then, the resulted solution was transferred to a 50 mL Teflon-lined stainless-steel autoclave and heated at 120 °C in an oven for 72 h. The precipitate was collected by centrifugation, washed with ethanol and dried under vacuum at 60 °C for 12 h.

Synthesis of BTCA-HZ-MesoCOF:

20 mg of BTCA (0.123 mmol), 10.6 μL HZ (0.219 mmol) and 180 mg of PEO-PS were dissolved in 2.0 mL DIO. 6.0 mL water was added to trigger the reaction. The mixture was stirred at 600 rpm for 12 h at room temperature. The resultant spherical BTCA-HZ-MesoCOF precursor was collected by centrifugation washed with THF three times. BTCA-HZ-MesoCOF was obtained after solvothermal reaction, employing a procedure analogous to that utilized for the preparation of BTCA-PD-MesoCOF. Using different amounts of DIO and water (2.0 mL DIO, 2.0 mL water and 100 μL aqueous acetic acid (3M) and employing a procedure analogous to that utilized for the preparation of BTCA-PD-MesoCOF, we obtained dendritic BTCA-HZ-MesoCOF.

Synthesis of BTCA-TAPB-MesoCOF:

20 mg of BTCA (0.123 mmol), 43 mg of TAPB (0.123 mmol) and 180 mg of PEO-PS were dissolved in 11.75 mL DIO. 2.25 mL water was added to trigger the reaction. The mixture was stirred at 600 rpm for 12 h at room temperature. The resultant spherical BTCA-TAPB-MesoCOF precursor was collected by centrifugation, washed with THF three times. BTCA-TAPB-MesoCOF was obtained after solvothermal reaction,[1] employing a procedure analogous to that utilized for the preparation of BTCA-PD-MesoCOF. Using different amounts of DIO and water (10.5 mL DIO and 3.5 mL water)

and employing a procedure analogous to that utilized for the preparation of BTCA-PD-MesoCOF, we obtained dendritic BTCA-TAPB-MesoCOF.

Synthesis of PDA-TAPB-MesoCOF:

37 mg of PDA (0.278 mmol), 64 mg of TAPB (0.185 mmol) and 180 mg of PEO-PS were dissolved in 17.0 mL DIO. 3.0 mL water was added to trigger the reaction. The mixture was stirred at 600 rpm for 12 h at room temperature. The resultant spherical PDA-TAPB-MesoCOF precursor was collected by centrifugation, washed with THF three times. PDA-TAPB-MesoCOF was obtained after solvothermal reaction,[2] employing a procedure analogous to that utilized for the preparation of BTCA-PD-MesoCOF. Using different amounts of DIO and water (15.25 mL DIO and 4.75 mL water) and employing a procedure analogous to that utilized for the preparation of BTCA-PD-MesoCOF, we obtained dendritic PDA-TAPB-MesoCOF.

Synthesis of PDA-TMT-MesoCOF:

41 mg of PDA (0.306 mmol), 25 mg of TMT (0.203 mmol) and 180 mg of PEO-PS were dissolved in 5.25 mL DIO. 0.75 mL water and 2.1 mL of 1M NaOH were added to trigger the reaction. The mixture was stirred at 600 rpm for 12 h at room temperature. The resultant spherical PDA-TMT-MesoCOF nanospheres were collected by centrifugation, washed with THF three times. Using different amounts of DIO and water (5.25 mL DIO, 0.75 mL water and 3.1 mL 1M of NaOH and employing a procedure analogous to that utilized for the preparation of PDA-TMT-MesoCOF, we obtained dendritic PDA-TMT-MesoCOF nanospheres.

PDA-TMT-MesoCOF/PDA-TMT-COF interphase preparation:

The COF powder and PVDF binder (4:1 by mass) were dispersed in N-methyl-2-pyrrolidone (NMP) to form a homogeneous slurry. After coating onto Zn foil, the electrodes were dried at 60 °C for 10 h, yielding COF@Zn electrodes (PDA-TMT-MesoCOF@Zn and PDA-TMT-COF@Zn).

Electrochemical measurements:

Zn||Zn symmetric cells were assembled using identical Zn anodes (PDA-TMT-MesoCOF@Zn, PDA-TMT-COF@Zn, or bare Zn; 100 μm thick and 12 mm in diameter) as both electrodes. A glass fiber separator (19 mm in diameter) soaked with 120 μL of 2 M $ZnSO_4$ aqueous electrolyte was used, and the cells were assembled in 2032-type coin cells. Galvanostatic cycling of Zn||Zn symmetric cells was conducted

on a Neware BTS-4000 battery tester. Coulombic efficiency was evaluated using asymmetric Zn||Cu cells, in which Cu mesh served as the counter electrode. Corrosion behavior was assessed by linear sweep voltammetry (LSV) over a potential range of −0.3 to 0.3 V versus the open-circuit potential at a scan rate of 1 mV s^{-1}. Chronoamperometry measurements were performed at an overpotential of −150 mV to evaluate Zn^{2+} diffusion behavior. Electrochemical impedance spectroscopy (EIS) was carried out using an electrochemical workstation in the frequency range from 100 kHz to 100 mHz. Zn||I_2 full cells were assembled using Ti foil as the current collector, the modified Zn anode, and 2 M $ZnSO_4$ aqueous electrolyte. Cyclic voltammetry (CV) of Zn||I_2 full cells was recorded between 0.5 and 1.6 V at a scan rate of 0.1 mV s^{-1}. All cells were assembled under ambient air conditions.

Electrostatic repulsion tests toward polyiodides

Preparation of Zn $(I_3)_2$ solution solution:Iodine (I_2) and potassium iodide (KI) with a molar ratio of 2:1 were dissolved in 2 M $ZnSO_4$ to prepare a Zn $(I_3)_2$ solution with a concentration of 4 mM.

To evaluate the electrostatic repulsion effect toward polyiodides, a pristine cellulose nanofiber (CMC) membrane was prepared by vacuum filtration of 5 mL of a CMC solution (4 mg mL^{-1}) as a control. For composite membranes, 10 mg of PDA-TMT-COF or PDA-TMT-MesoCOF was dispersed in 5 mL of the CMC solution (4 mg mL^{-1}), followed by vacuum filtration to obtain PDA-TMT-COF@CMC and PDA-TMT-MesoCOF@CMC membranes. These membranes were employed to assess the exclusion behavior of polyiodides arising from electrostatic interactions.

Computational methods：

The molecular electrostatic potential (ESP) charges of PDA-TMT-COF were determined using the DMol³ module implemented in Materials Studio, employing the generalized gradient approximation (GGA) with the Perdew–Burke–Ernzerhof (PBE) exchange–correlation functional.[3] The calculations were carried out within the framework of density functional theory (DFT) using the projector augmented plane-wave (PAW) method, as implemented in the Vienna ab initio simulation package.[4] The exchange-correlation potential is approximated by the generalized gradient approximation (GGA) proposed by Perdew, Burke, and Ernzerhof.[5] To account for long-range van der Waals interactions, the DFT-D3 method by Grimme with a zero-damping function is employed.[6] The plane wave cut-off energy is set at 450 eV, and

the energy convergence criterion for the iterative solution of the Kohn-Sham equations is set to 10^{-5} eV. A vacuum region of 15 Å is included perpendicular to the slab to prevent artificial interactions between periodic images. The Monkhorst-Pack scheme, with a K-point mesh density of 0.08 π/Å, is used for all DFT calculations. Structural relaxation is performed until the residual forces on atoms are less than 0.05 eV/Å. The adsorption energy (E_{ads}) of $Zn(H_2O)_n^{2+}$ (where n = 0, 2, 4) on the substratewas calculated using the following equation: $E_{ads} = E_{total} - E_{substrate} - E_{ion}$, where E_{total} is the total energy of the substrate with the adsorbed hydrated zinc ion, $E_{substrate}$ is the energy of the isolated substrate, and E_{ion} is the energy of the isolated $Zn(H_2O)_n^{2+}$ complex.

2. Supplementary Figures

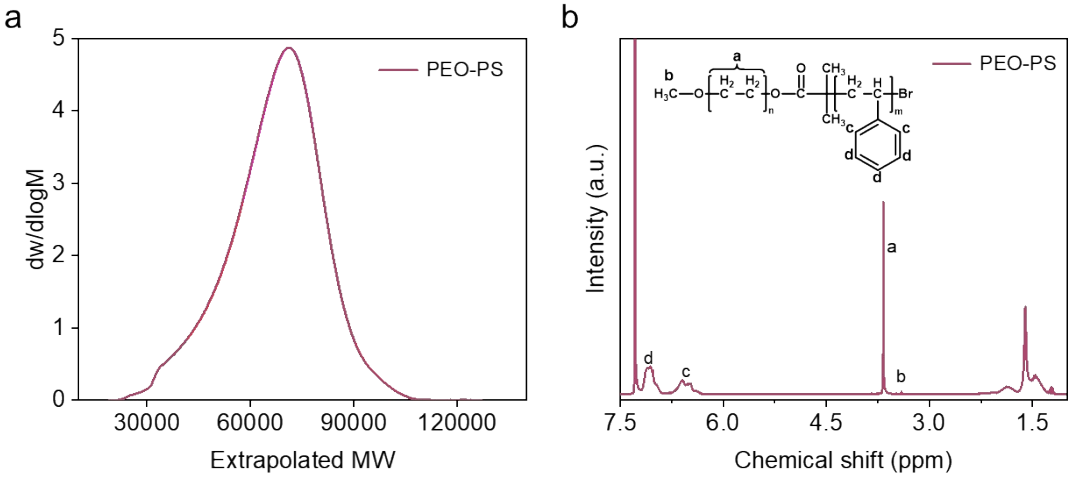

Figure S1 (a) Gel permeation chromatography (GPC) spectrum and (b) ^{1}H NMR hydrogen spectrum of PEO-PS.

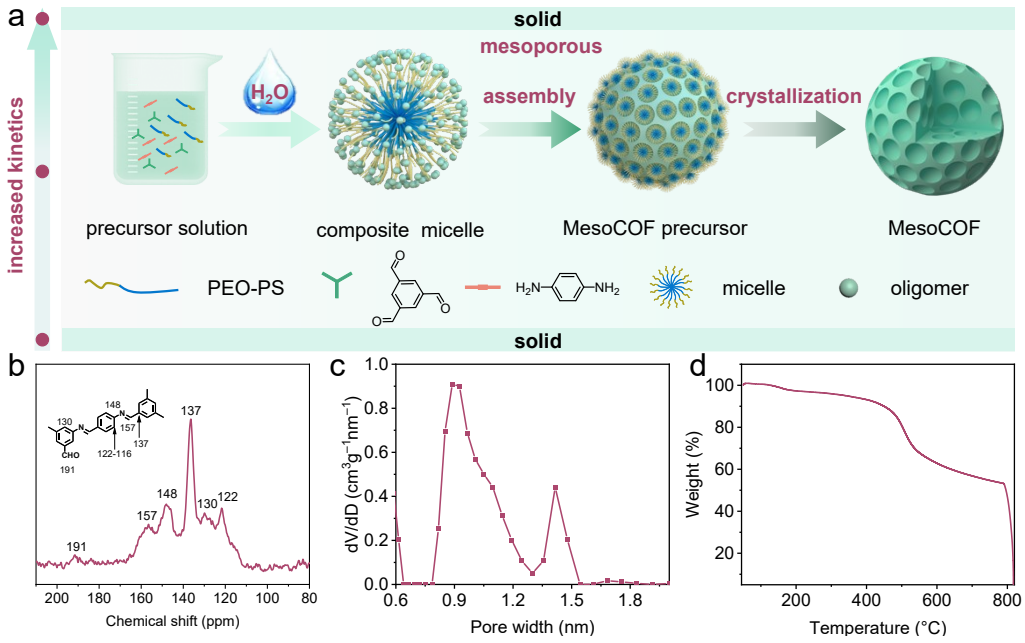

Figure S2 (a) Schematic illustration of the synthesis of BTCA-PD-MesoCOF by kinetics-mediated micelle assembly strategy. (b) solid-state ^{13}C NMR spectrum of BTCA-PD-MesoCOF. (c) Pore width distribution data calculated by the QSDFT model, (d) TGA curve of BTCA-PD-MesoCOF.

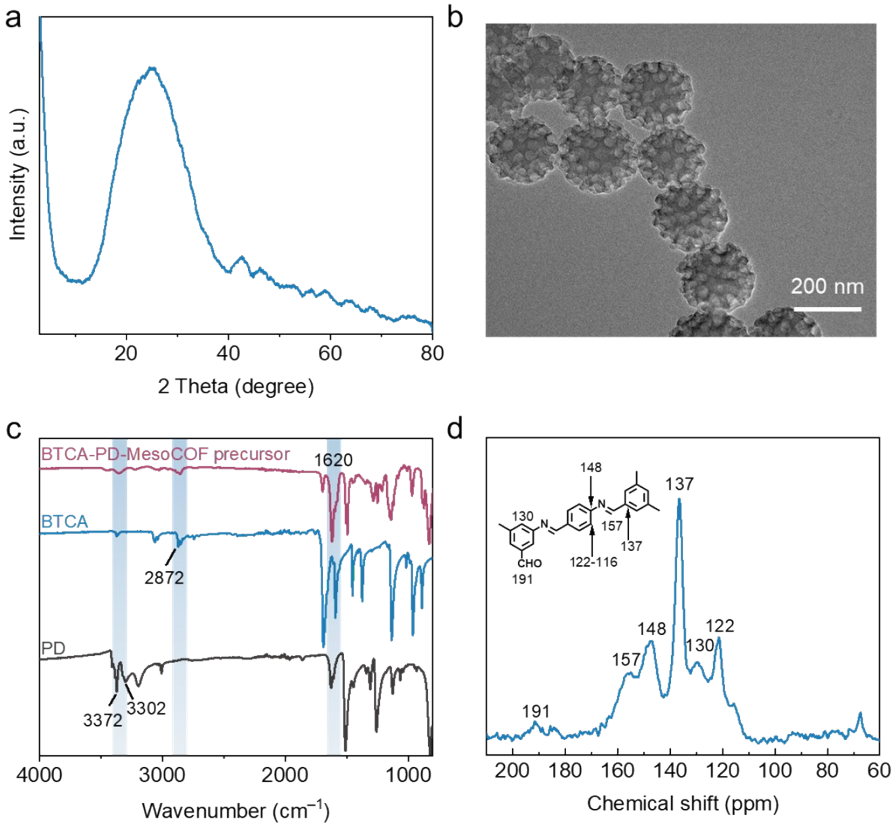

Figure S3 (a) XRD pattern and (b) TEM image of the BTCA-PD-MesoCOF precursor. (c) FT-IR spectra of the BTCA-PD-MesoCOF precursor, BTCA and PD. (d) Solid-state ^{13}C NMR spectrum of the BTCA-PD-MesoCOF precursor.

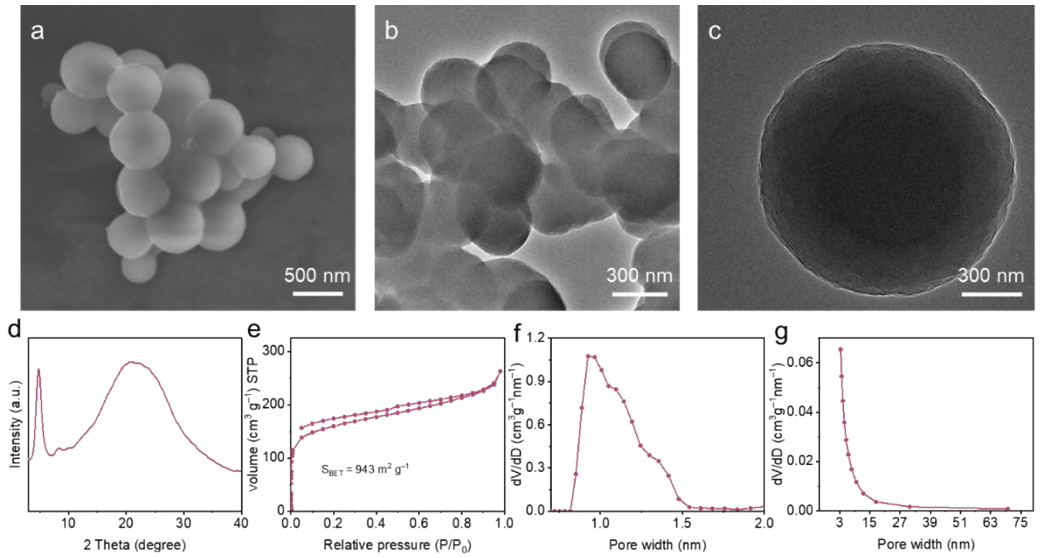

Figure S4 (a-c) SEM and TEM images, (d) XRD pattern, (e) N_2 adsorption–desorption isotherms and (f, g) pore size distribution curve of the solid BTCA-PD-COF spheres synthesized with 5 vol% H_2O.

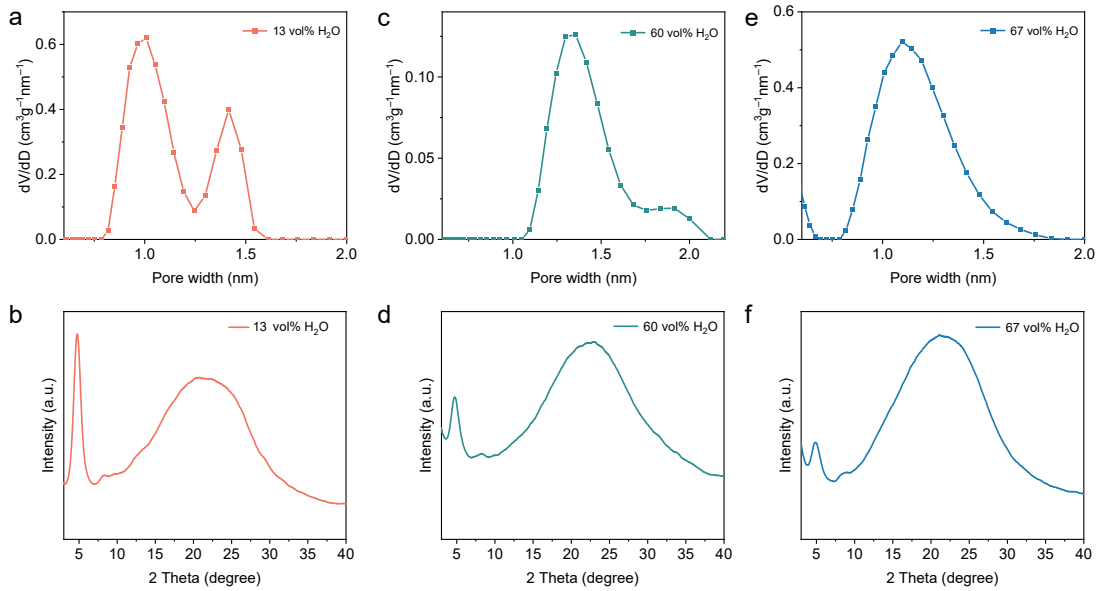

Figure S5 Pore width distribution data calculated by the QSDFT model and XRD patterns of BTCA-PD-MesoCOFs prepared with different amounts of H_2O. (a, b) 13 vol%, (c, d) 60 vol% and (e, f) 67 vol%.

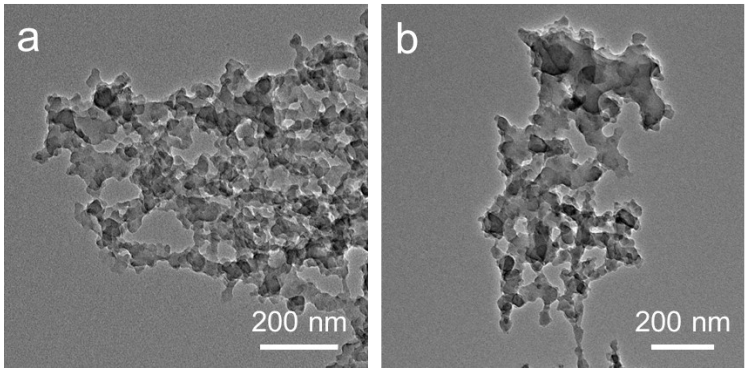

Figure S6 (a, b) TEM images of small BTCA-PD-COF nanoparticles prepared with 91 vol% H_2O.

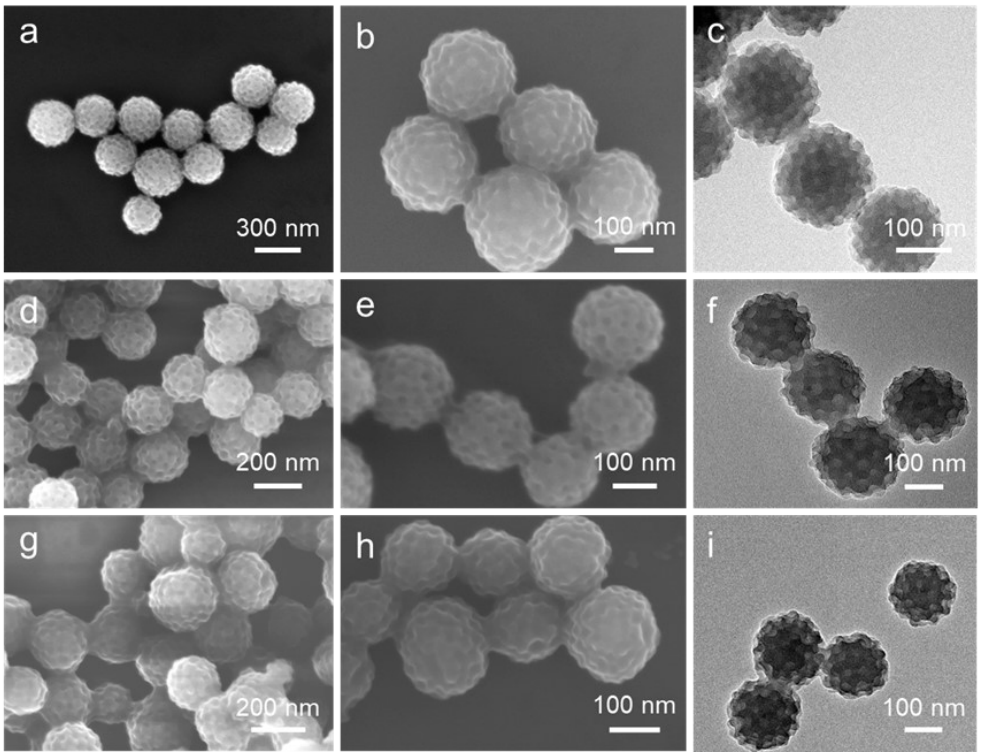

Figure S7 SEM and TEM images of the BTCA-PD-MesoCOFs synthesized under different concentrations of PEO-PS. (a–c) 60 mg mL^{-1}, (d–f) 120 mg mL^{-1} and (g–i) 240 mg mL^{-1}.

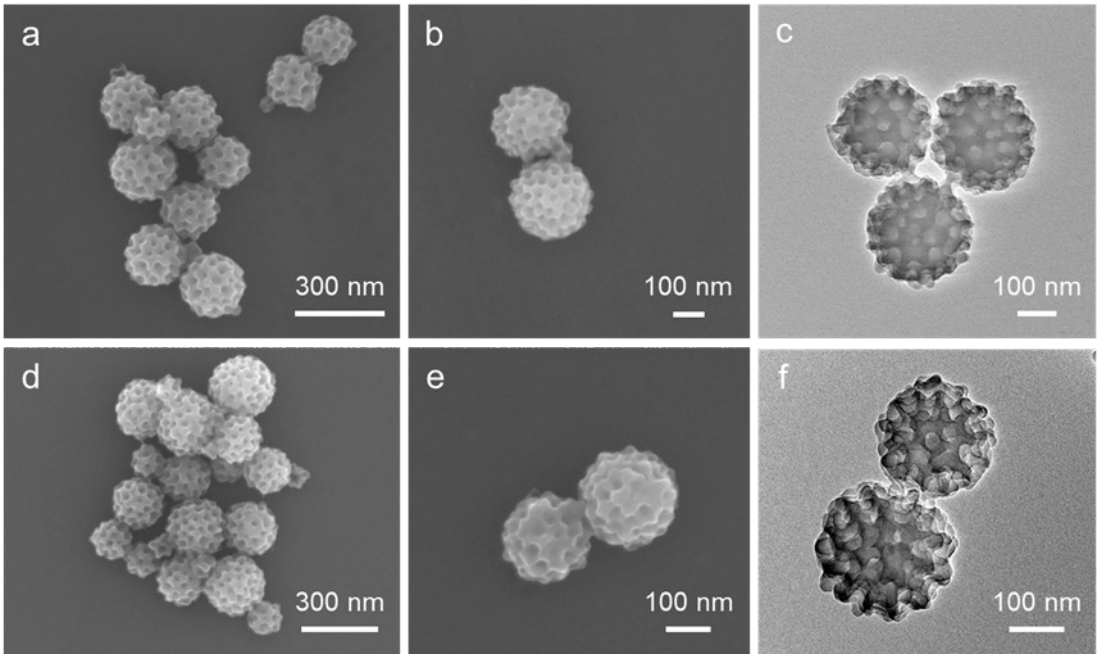

Figure S8 SEM and TEM images of the BTCA-PD-MesoCOFs synthesized at different stirring rates. (a–c) 900 rpm and (d–f) 1200 rpm.

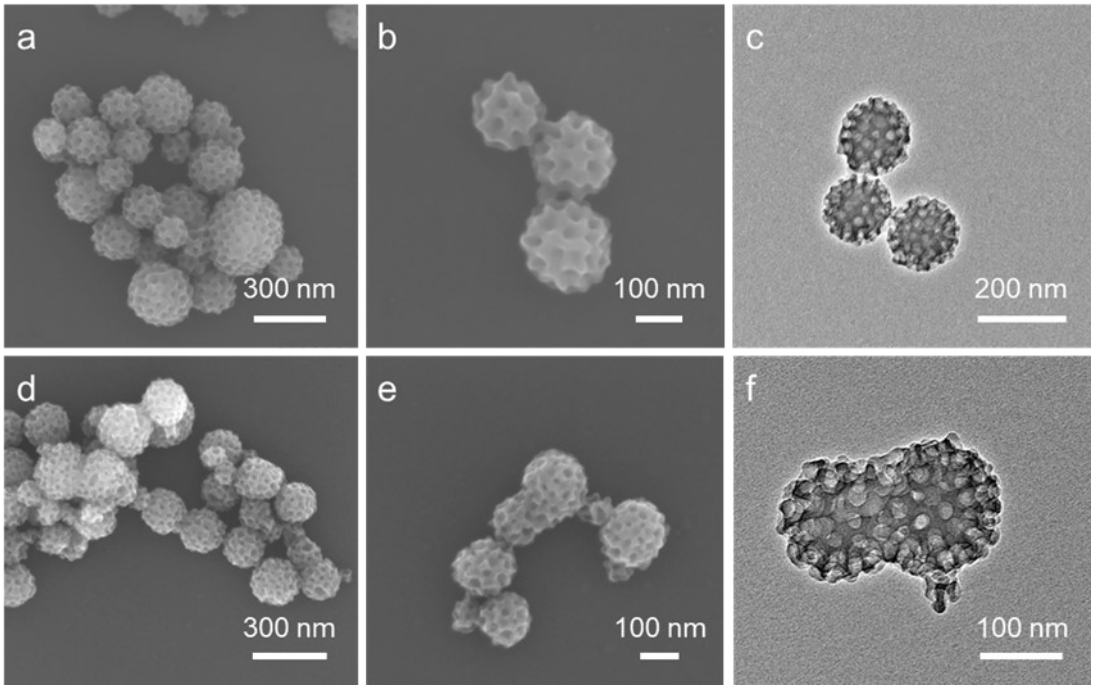

Figure S9 SEM and TEM images of the BTCA-PD-MesoCOFs synthesized at different temperatures. (a–c) 60 °C and (d–f) 90 °C

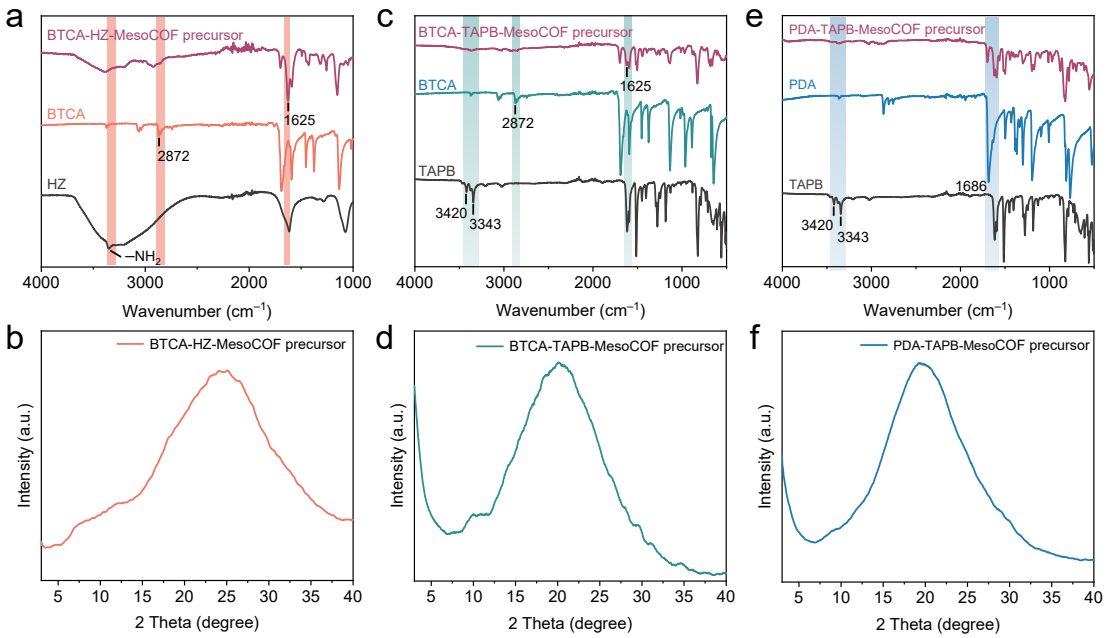

Figure S10 FT-IR spectra and XRD patterns of MesoCOF precursors with different organic linkages. (a, b) BTCA-HZ-MesoCOF precursor, (c, d) BTCA-TAPB-MesoCOF precursor and (e, f) PDA-TAPB-MesoCOF precursor.

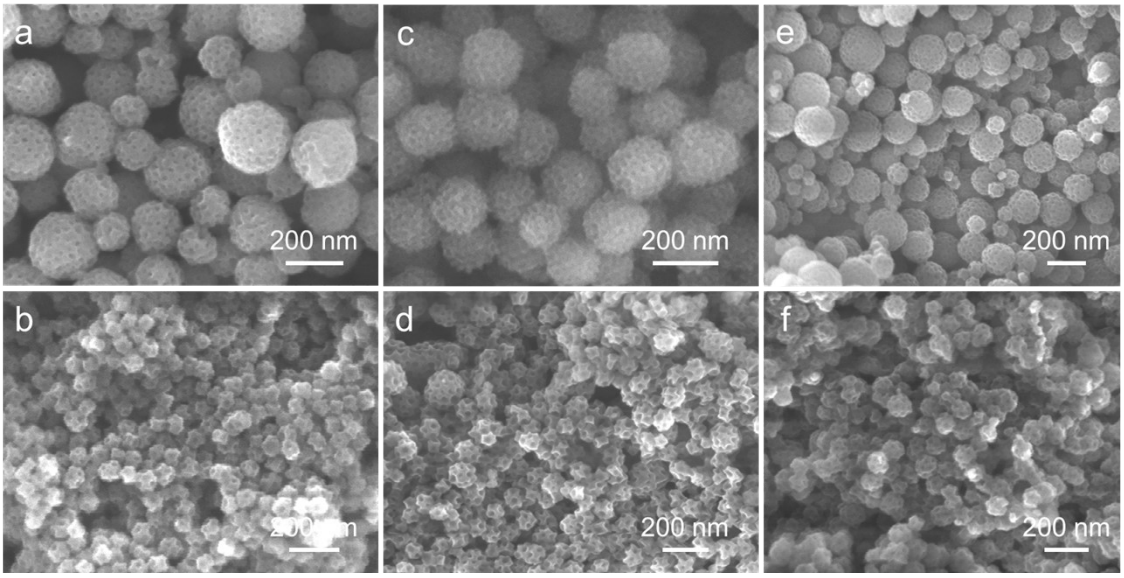

Figure S11 SEM images of spherical and dendritic MesoCOF precursors with different organic linkages. (a, b) BTCA-HZ-MesoCOF precursor, (c, d) BTCA-TAPB-MesoCOF precursor and (e, f) PDA-TAPB-MesoCOF precursor.

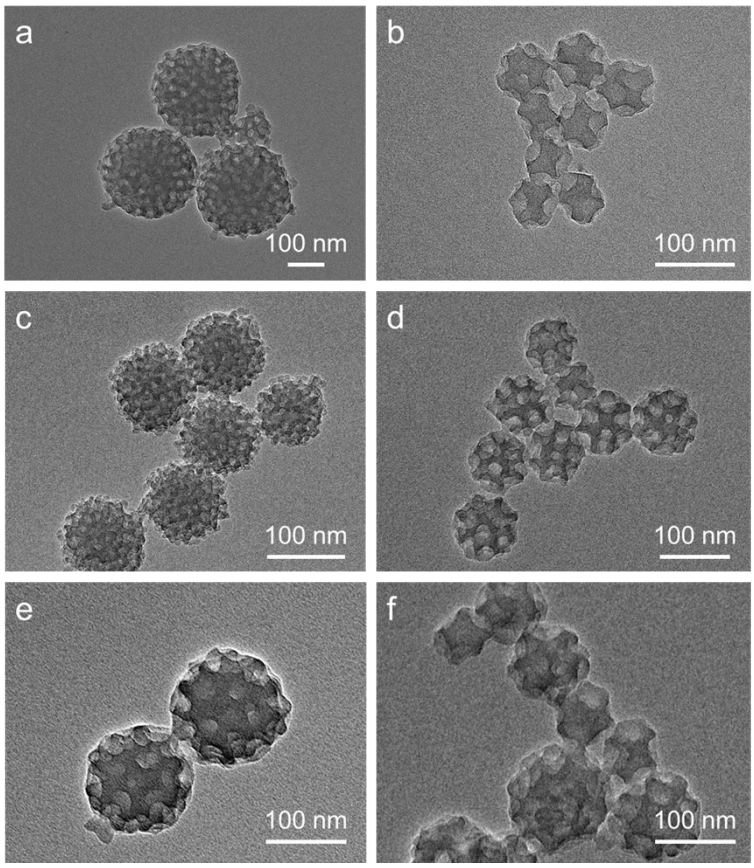

Figure S12 TEM images of spherical and dendritic MesoCOF precursors with different organic linkages. (a, b) BTCA-HZ-MesoCOF precursor, (c, d) BTCA-TAPB-MesoCOF precursor and (e, f) PDA-TAPB-MesoCOF precursor.

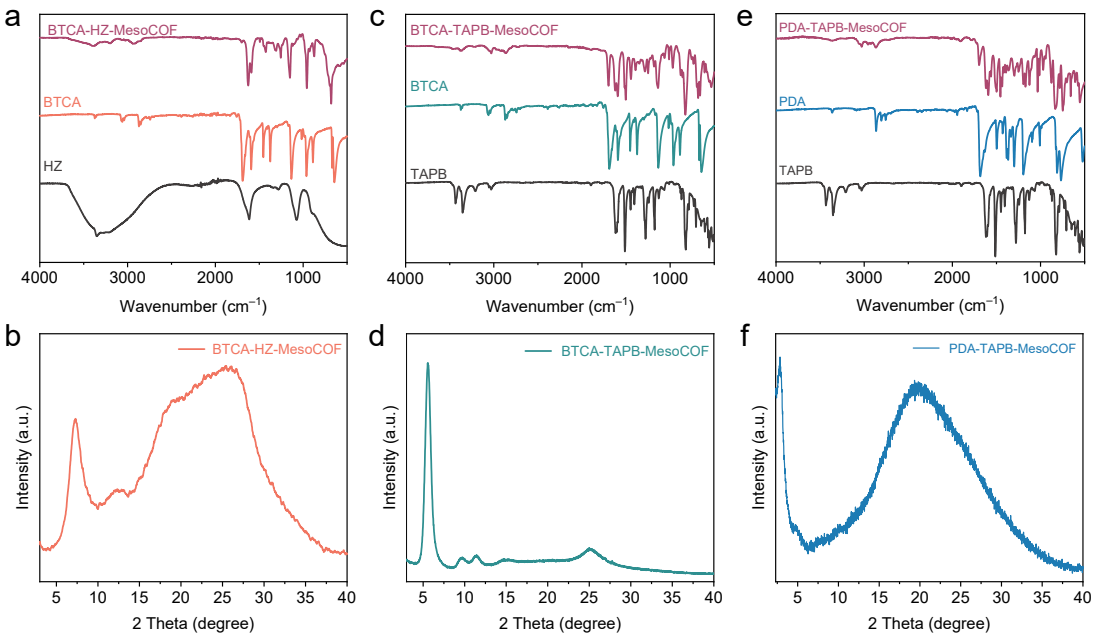

Figure S13 FT-IR spectra and XRD patterns of MesoCOFs with different organic linkages. (a, b) BTCA-HZ-MesoCOF, (c, d) BTCA-TAPB-MesoCOF and (e, f) PDA-TAPB-MesoCOF.

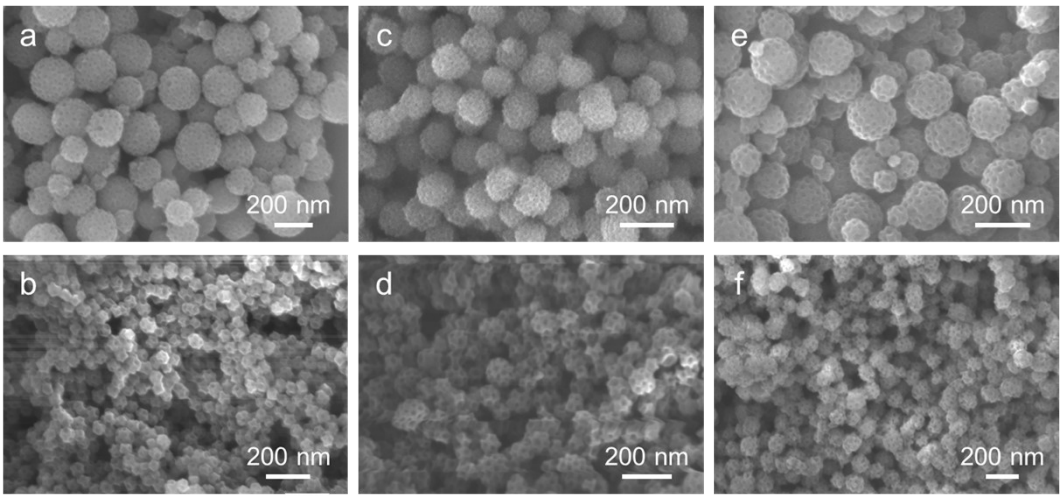

Figure S14 SEM images of spherical and dendritic MesoCOFs with different organic linkages. (a, b) BTCA-HZ-MesoCOF, (c, d) BTCA-TAPB-MesoCOF and (e, f) PDA-TAPB-MesoCOF.

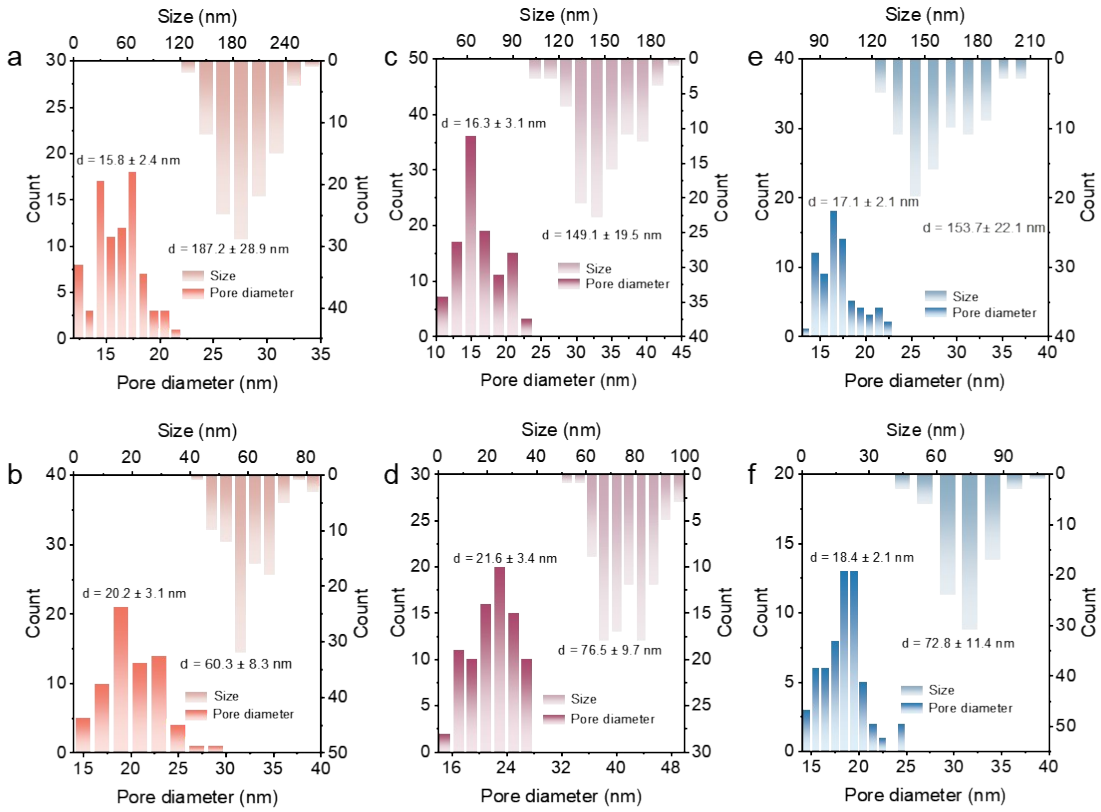

Figure S15 The graphs present the distributions of the pore diameters and particle sizes obtained by the TEM images. (a, b) The spherical and dendritic BTCA-HZ-MesoCOFs. (c, d) The spherical and dendritic BTCA-TAPB-MesoCOFs. (e, f) The spherical and dendritic PDA-TAPB-MesoCOFs.

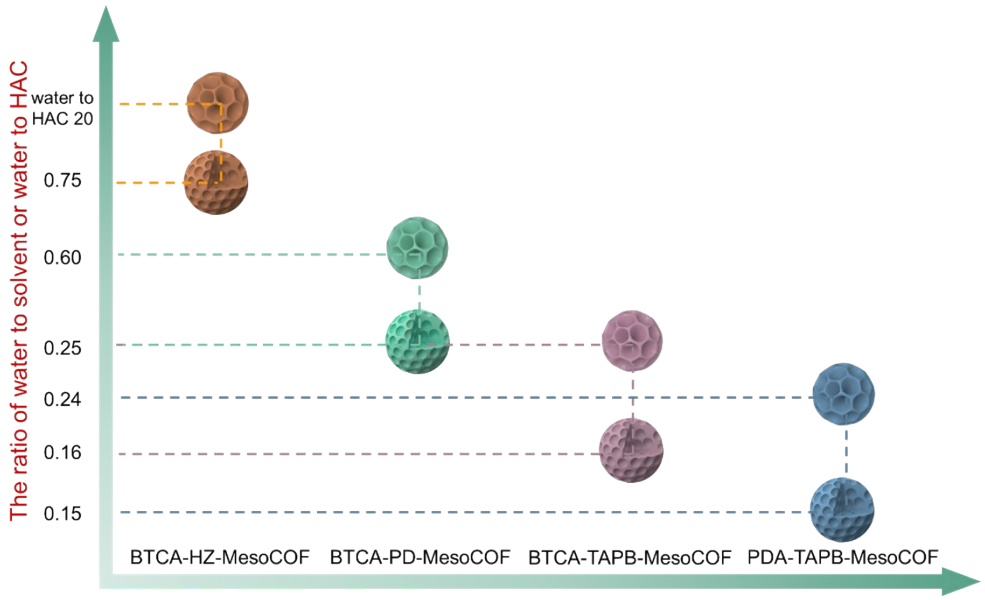

Figure S16 Schematic illustration of the water/solvent ratios and catalyst of the same mesoporous structure for different monomers.

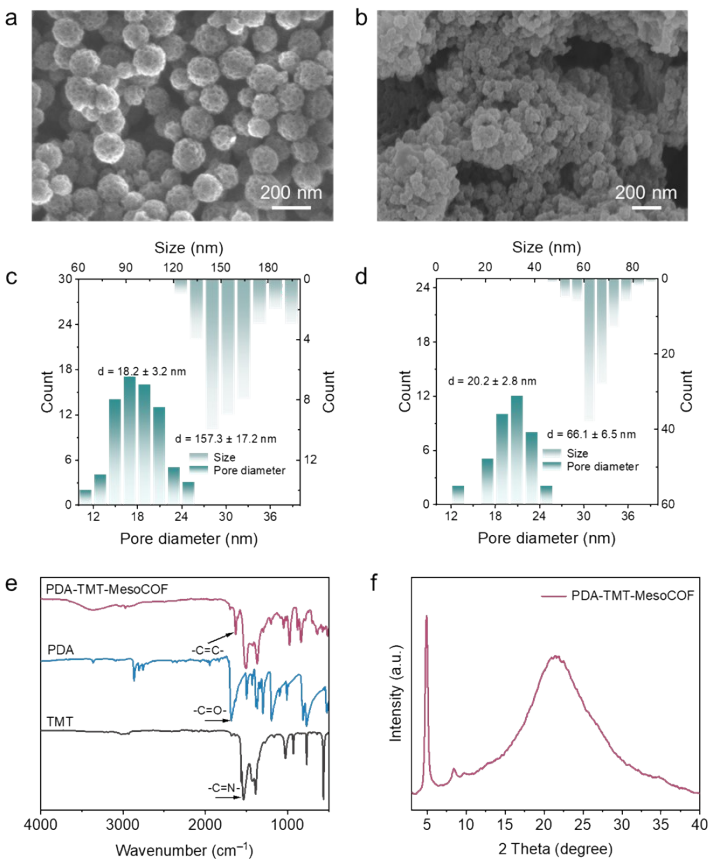

Figure S17 (a, b) SEM images of spherical and dendritic PDA-TMT-MesoCOF and the corresponding pore diameter and particle size distributions from TEM analysis. (c, d) FT-IR spectra and XRD patterns of PDA-TMT-MesoCOF.

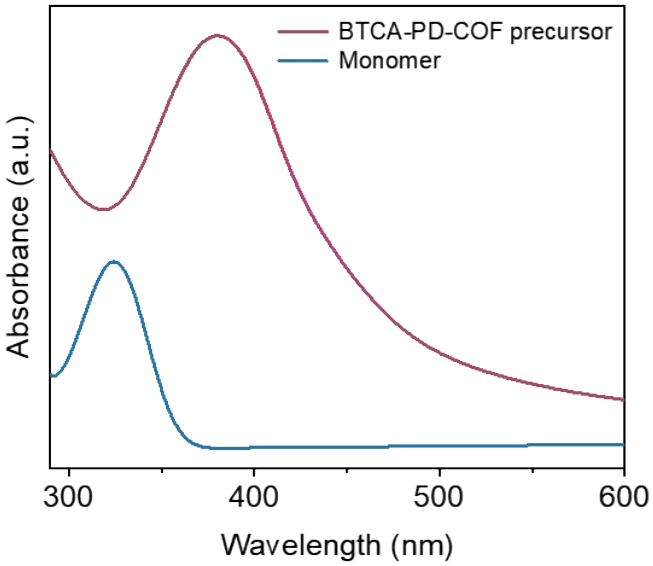

Figure S18 UV-Vis absorption spectra of the monomer mixture and BTCA-PD-COF precursor.

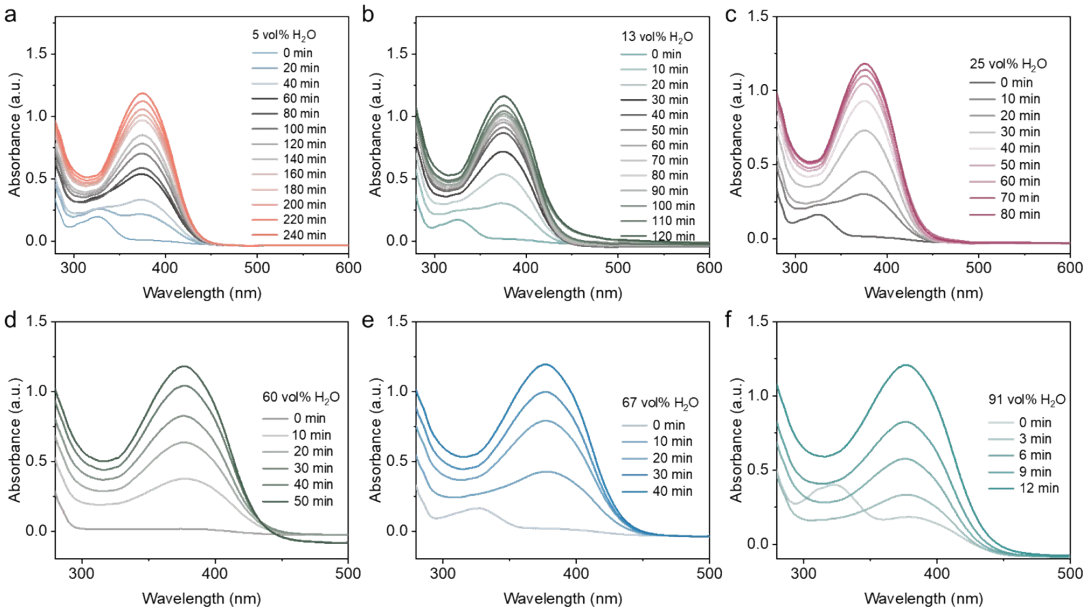

Figure S19 Time-dependent UV−Vis spectrophotometric measurements of the BTCA-PD-COF precursors prepared with different amounts of water. (a) 5 vol%, (b) 13 vol%, (c) 25 vol%, (d) 60 vol%, (e) 67 vol% and (f) 91 vol%.

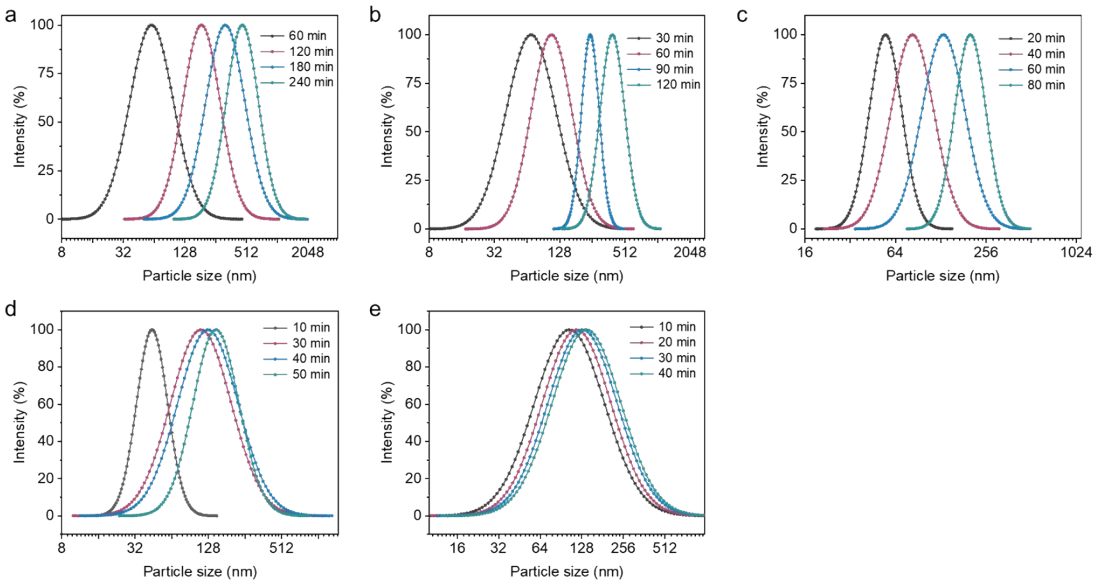

Figure S20 Time-dependent DLS measurements of BTCA-PD-COF precursors prepared with different water contents: (a) 5 vol%, (b) 13 vol%, (c) 25 vol%, (d) 60 vol%, and (e) 67 vol%.

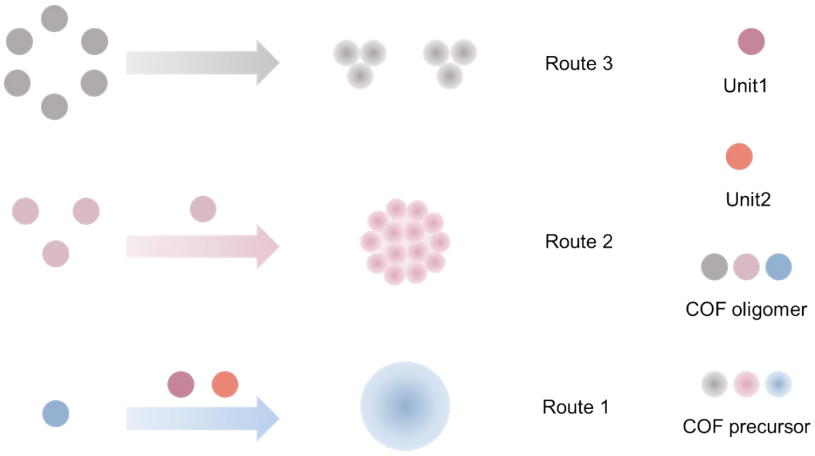

Figure S21 Schematic illustration of the kinetics-mediated micelle assembly growth routes.

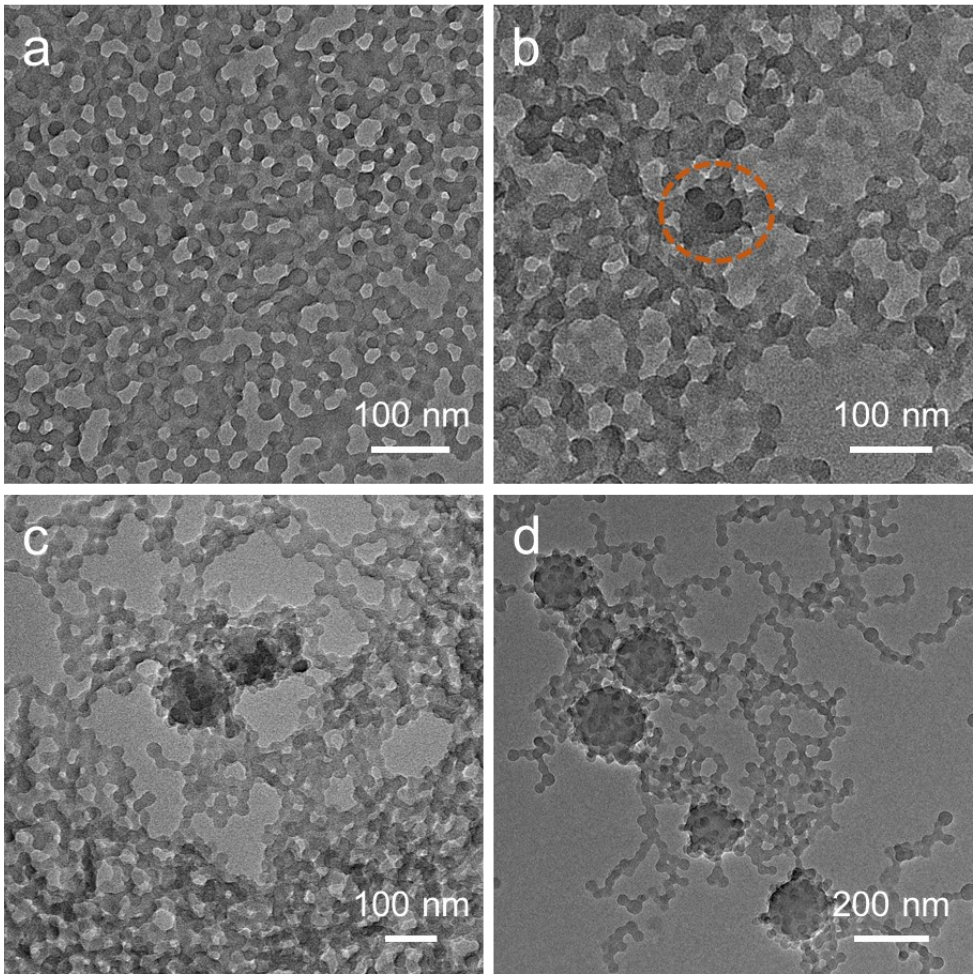

Figure S22 TEM images of the BTCA-PD-MesoCOF precursors with spherical mesopores synthesized in 25 vol% water obtained at different reaction times. (a) 20 min, (b) 40 min, (c) 60 min and (d) 80 min.

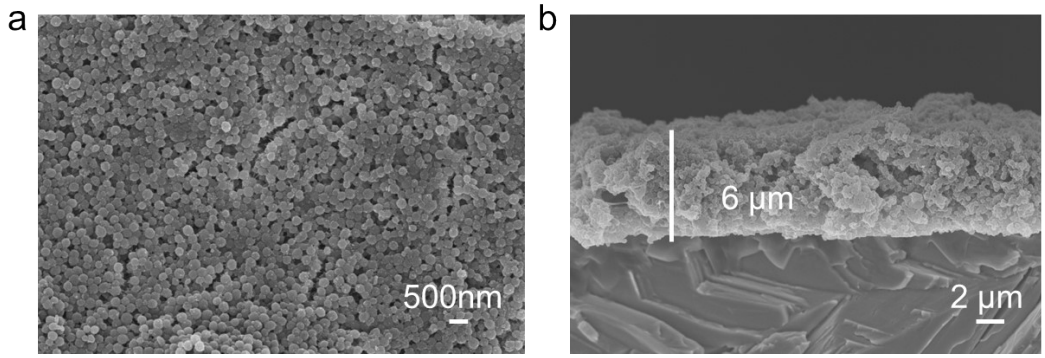

Figure S23 (a) Top-view and (b) cross-sectional SEM images of the PDA-TMT-MesoCOF@Zn electrode.

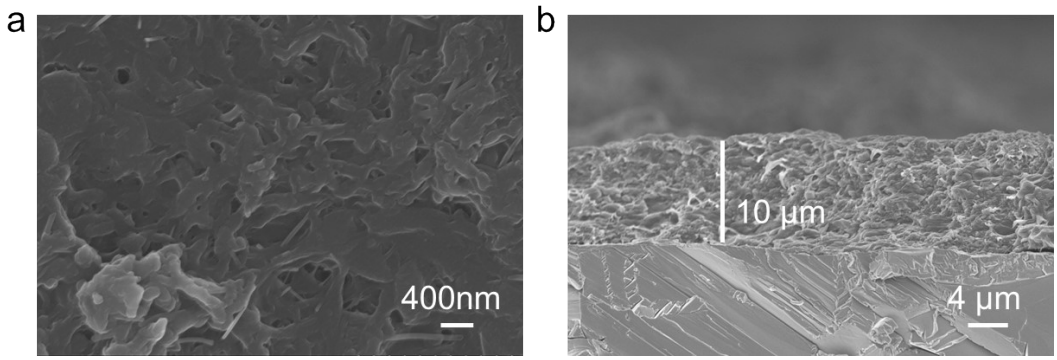

Figure S24 (a) Top-view and (b) cross-sectional SEM images of the PDA-TMT-COF@Zn electrode.

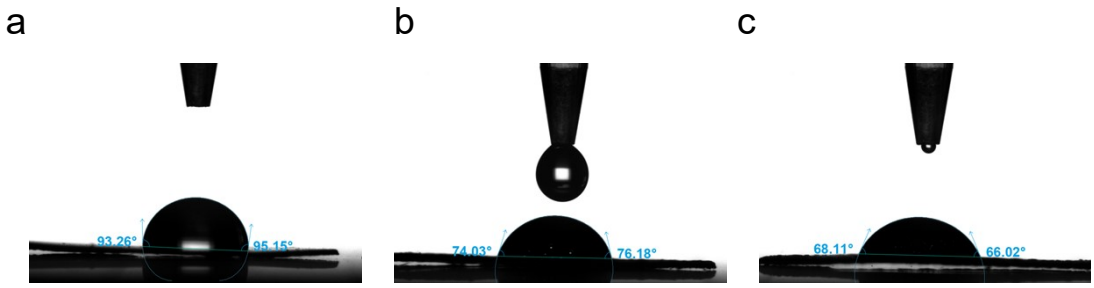

Figure S25 (a–c) Contact angle images of (a) bare Zn, (b) PDA-TMT-COF@Zn, and (c) PDA-TMT-MesoCOF@Zn electrodes.

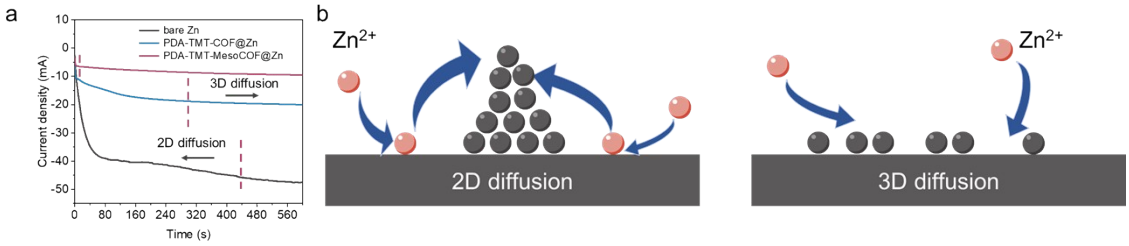

Figure S26 (a) CA measurements of Zn||Zn symmetric cells with PDA-TMT-MesoCOF@Zn, PDA-TMT-COF@Zn and bare Zn electrodes under −150 mV overpotential. (b) Schematic illustration of zinc ion diffusion and plating process on PDA-TMT-MesoCOF@Zn and bare Zn anodes. For bare Zn and PDA-TMT-COF@Zn, Zn^{2+} ions predominantly undergo lateral surface diffusion during the two-dimensional diffusion stage and preferentially deposit at energetically favorable sites due to the tip effect, which promotes dendritic growth. In contrast, the PDA-TMT-MesoCOF@Zn anode, benefiting from the Zn^{2+} affinity of triazine units, enables more homogeneous Zn^{2+} ion diffusion and favors a three-dimensional deposition behavior.

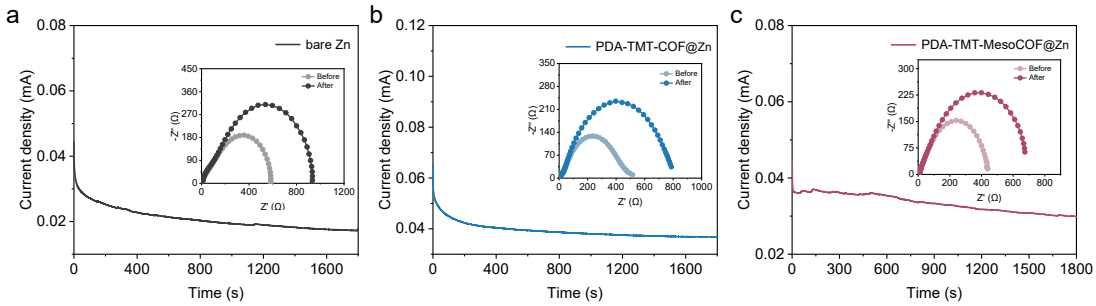

Figure S27 (a–c) Chronoamperometric (CA) responses of Zn||Zn symmetric cells with (a) bare Zn, (b) PDA-TMT-COF@Zn, and (c) PDA-TMT-MesoCOF@Zn electrodes. Insets show the corresponding EIS spectra recorded before and after polarization.

Here R_{el}^{0} and R_{el}^{s} represent the initial and steady-state interfacial impedances (obtained by fitting the impedance spectra). respectively, I_0 and I_s denote the initial and steady-state currents measured during the CA test, under an applied potential difference of ΔV

$$t_{Zn^{2+}} = \frac{I_s\left(\Delta V - I_0 R_{el}^{0}\right)}{I_0\left(\Delta V - I_s R_{el}^{s}\right)}$$

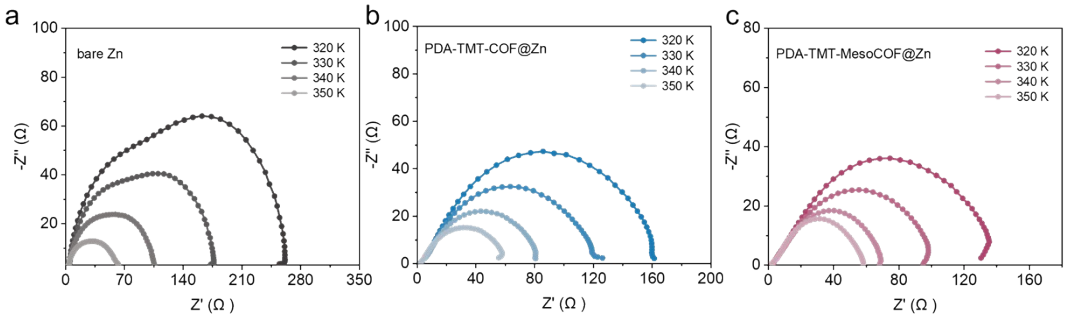

Figure S28 Electrochemical impedance spectra of Zn||Zn symmetric cells measured at different temperatures using (a) bare Zn, (b) PDA-TMT-COF@Zn, and (c) PDA-TMT-MesoCOF@Zn electrodes.

The desolvation energy barrier of hydrated Zn^{2+} was derived from the temperature-dependent charge-transfer resistance based on the Arrhenius relationship.

The desolvation energy barrier was calculated according to the Arrhenius equation

$$\ln\left(\frac{1}{R_{ct}}\right) = e^{-\frac{E_a}{RT}}$$

Where R_{ct} is the charge-transfer resistance, E_a is the activation energy, R is the gas constant, and T is the absolute temperature.

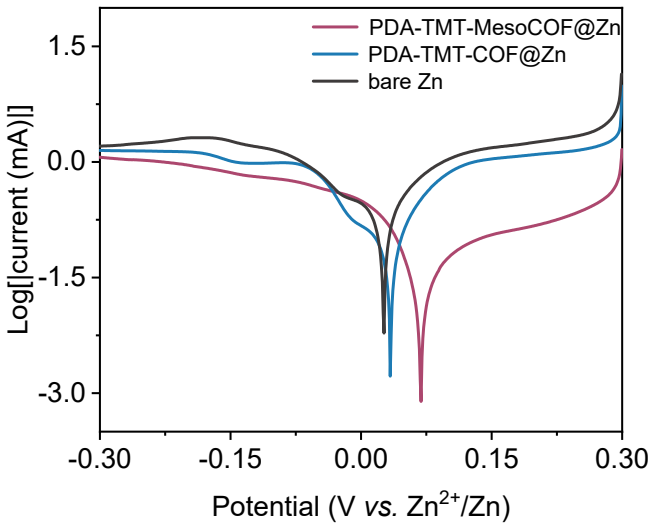

Figure S29 Tafel plots of bare Zn, PDA-TMT-COF@Zn, and PDA-TMT-MesoCOF@Zn anodes.

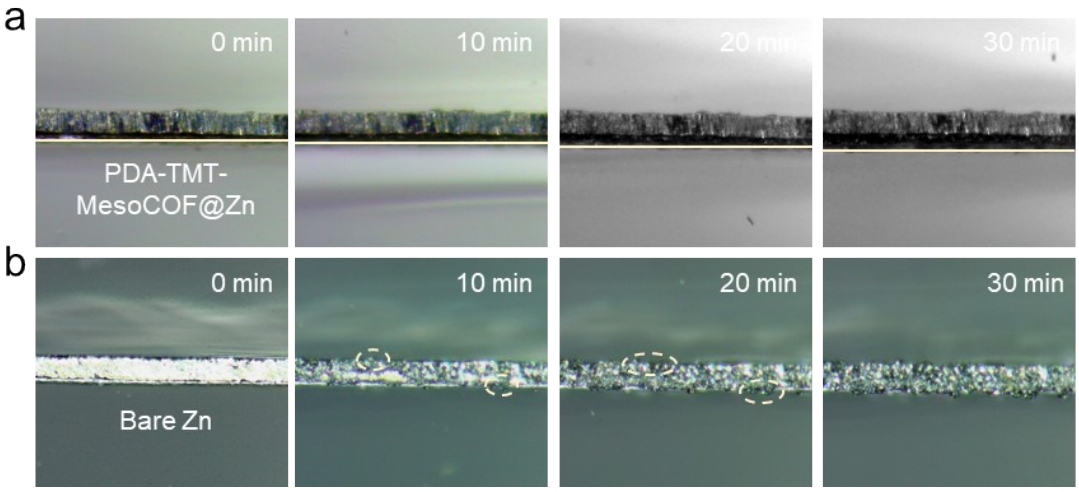

Figure S30 In situ optical microscopy images recorded during Zn^{2+} plating at a current density of 10 mA cm^{-2}.

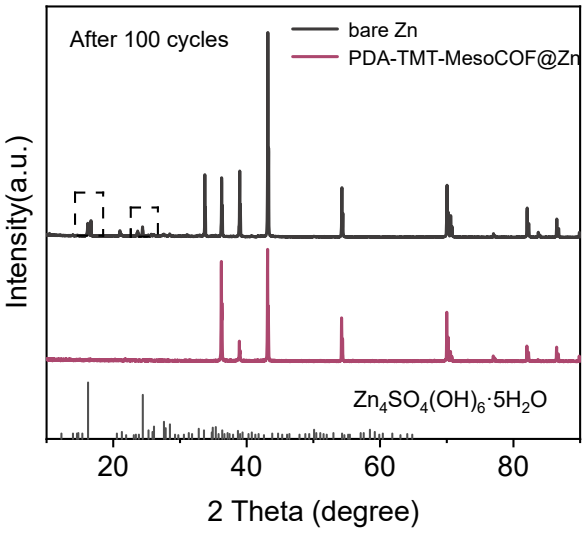

Figure S31 XRD patterns of cycled bare Zn and PDA-TMT-MesoCOF@Zn electrodes.

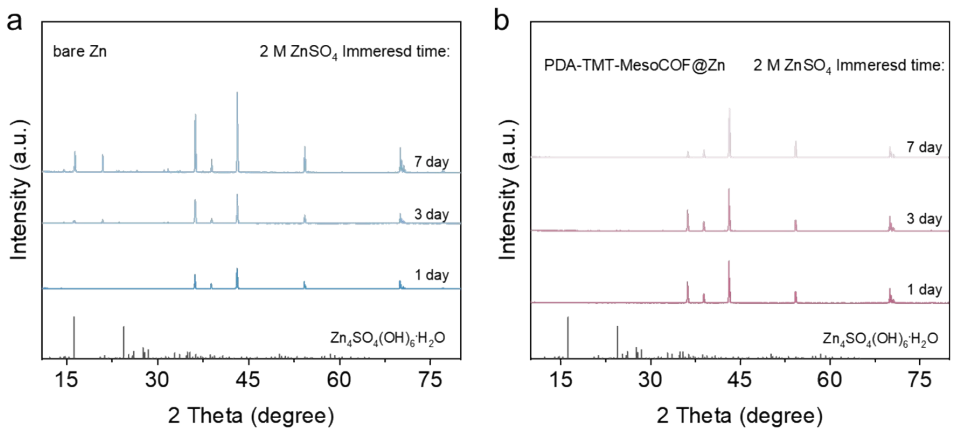

Figure S32 XRD patterns of bare Zn and PDA-TMT-MesoCOF@Zn anodes after immersion in 2 M $ZnSO_4$ electrolyte for 1, 3, and 7 days.

In this context, the PDA-TMT-MesoCOF layer should not be regarded as a dense water-proof barrier, but rather as a mesoporous ion-selective interphase. Its protection effect mainly arises from interfacial kinetic regulation, including facilitated Zn^{2+} desolvation/homogenized Zn^{2+} flux, suppressed polyiodide crossover, and reduced parasitic interfacial reactions. Consistent with this interpretation, the improved Tafel behavior, reduced $Zn_4SO_4(OH)_6{\cdot}5H_2O$ byproduct formation, and the static immersion results collectively confirm substantially mitigated self-corrosion on PDA-TMT-MesoCOF@Zn.

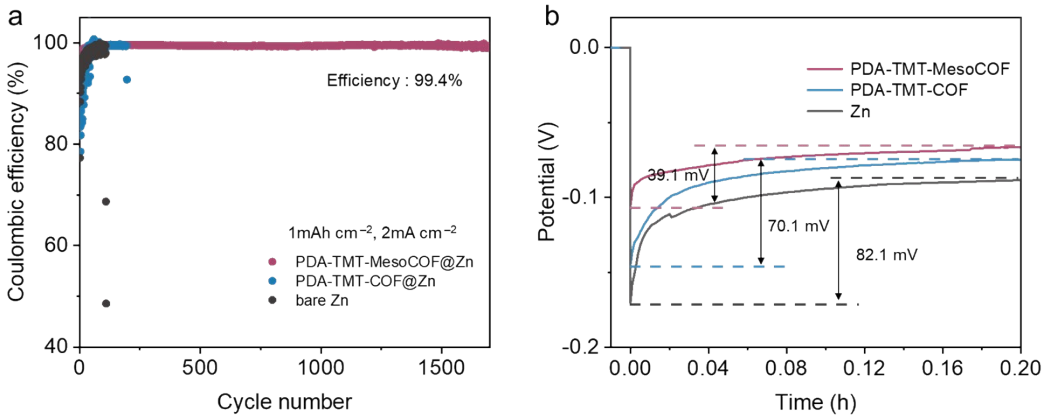

Figure S33 (a) Comparison of the Coulombic efficiencies (CE) of Zn plating and stripping in bare Zn||Cu, PDA-TMT-COF@Zn||Cu and PDA-TMT-MesoCOF@Zn||Cu cells. (b) Nucleation overpotentials of bare Zn, PDA-TMT-COF@Zn, and PDA-TMT-MesoCOF@Zn electrodes measured at a current density of 5 mA cm^{-2}.

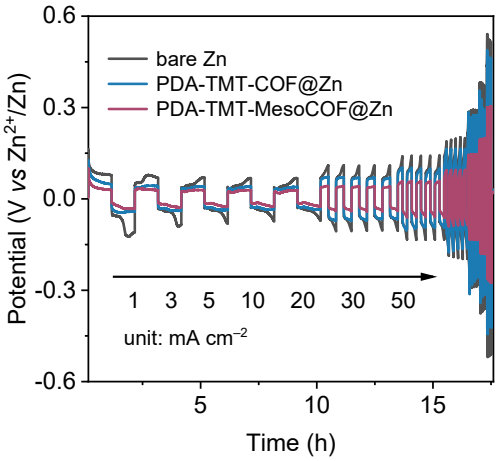

Figure S34 Rate performance of Zn||Zn symmetric cells with different Zn anodes at various current densities.

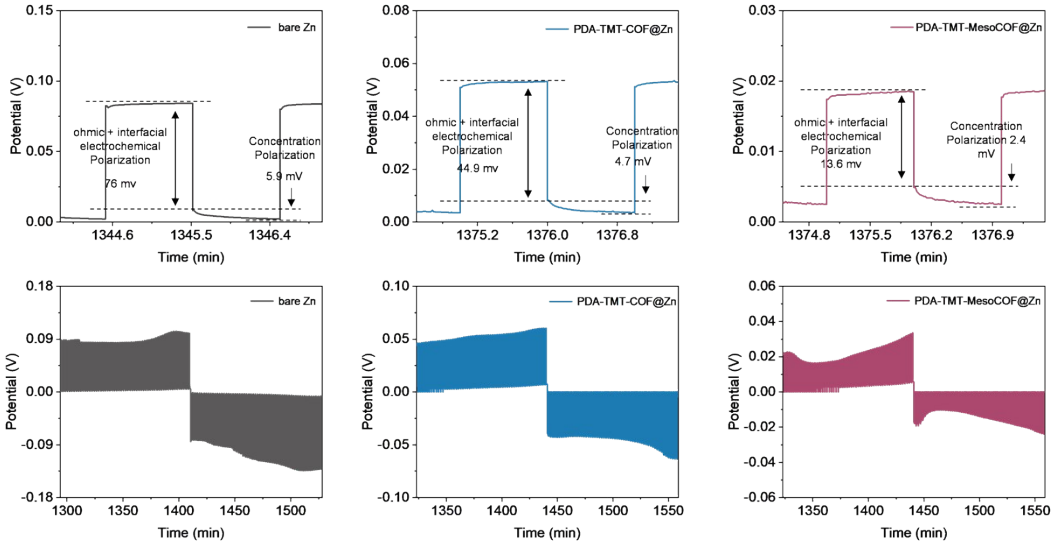

Figure S35 Galvanostatic Intermittent Titration Technique (GITT) profiles and the magnified voltage curves for bare Zn, PDA-TMT-COF@Zn and PDA-TMT-MesoCOF@Zn electrodes.

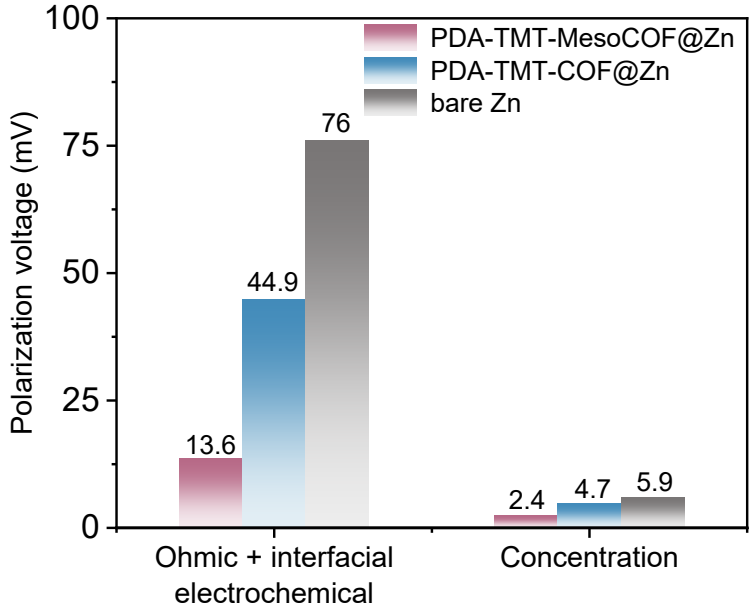

Figure S36 Contribution of the polarization voltage during a selected pulse/rest step in the charging process, as derived from GITT measurements.

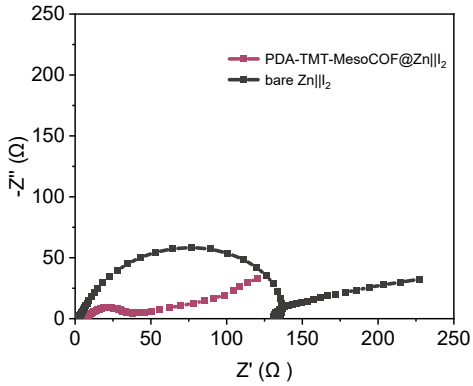

Figure S37 The Nyquist plots of bare Zn||I_2 and PDA-TMT-MesoCOF@Zn||I_2 full cells.

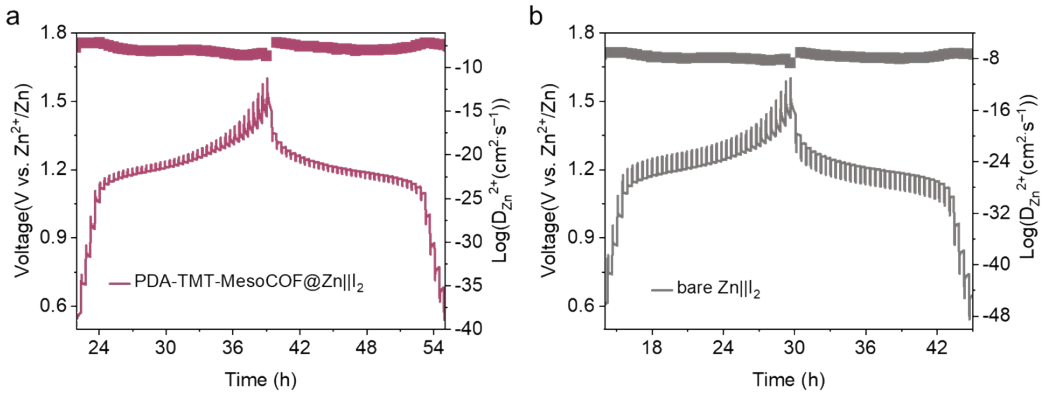

Figure S38 GITT curves and corresponding ionic diffusion coefficients of (a) PDA-TMT-MesoCOF@Zn||I_2 and (b) bare Zn||I_2 full cells.

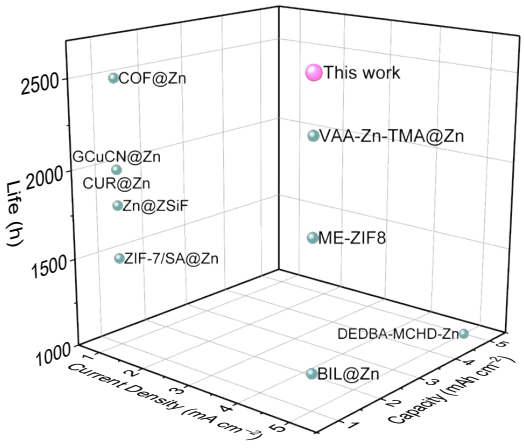

Figure S39 Benchmarking of the cycling stability of PDA-TMT-MesoCOF@Zn against state-of-the-art Zn anode protective layers in symmetric cells.

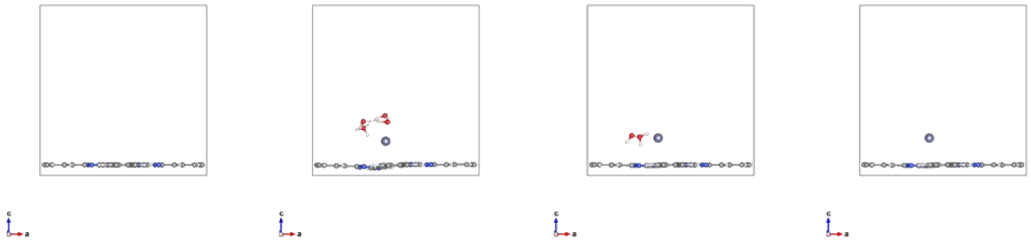

Figure S40 DFT-optimized binding geometries of bare PDA-TMT-COF and the corresponding adsorption states of $[Zn(H_2O)_4]^{2+}$, $[Zn(H_2O)_2]^{2+}$, and Zn^{2+} (left to right, bottom panel). Atom coloring: C (gray), N (blue), H (white), O (red), and Zn (purple).

3. Supplementary Tables

Table S1 Comparison of representative large-pore mesoporous COF synthesis strategies reported in the literature and this work.

Entry	Synthetic Strategy	Linkage	Pore size (nm)	Pore control	Compositional diversity	Ref.
1	Ligand extension	Imine	3.3	/	1 type	*7*
2	Ligand extension	Imine	3.2	/	1 type	*8*
3	Ligand extension	Boronate ester-linked	3.5, 6	/	1 type	*9*
4	Hard-templating	Imine	17-40	spherical	1 type	*10*
5	Hard-templating	Imine	7-40	spherical	1 type	*11*
6	Hard-templating	π-COF	35	spherical	1 type	*12*
7	Soft-templating (ionic bonding)	Imine	3.3-4.5	/	2 types	*13*
8	Soft-templating **kinetics-mediated micelle assembly strategy**	**Imine, ethylene**	**15.8–21.6**	**Spherical, dendritic, walnut-like**	**5 types**	**This work**

Table S2. Comparison of cycling stability and activation energy for PDA-TMT-MesoCOF@Zn with mesoporous interphase materials reported recently.

Interphase	**Cycling stability** (current density (mA cm^{-2})/capacity (mAh cm^{-2}) (life span (h))	E_a	Ref.
PDA-TMT-MesoCOF@Zn	**5-1 2700**	**17.85 KJ mol^{-1}**	**This work**
HMNVP/C@Zn	1-1 300	21.64 KJ mol^{-1}	14
NOPC-Zn	5-1 2400	/	15
PZT	5-1 1600	15.8 KJ mol^{-1}	16
F-Si@HMCS@Zn	5-0.5 2500	/	17
CeO_2-Zn	2-1 1500	/	18
HMCSST-Zn	3-3 1300	21.11 KJ mol^{-1}	19
Zn-TiO_2/NCDs5	5-2.5 1500	/	20
MCM41-Zn	1-1 1800	15.041 KJ mol^{-1}	21

Table S3. Comparison of cycling stability and activation energy for PDA-TMT-MesoCOF@Zn with COF-based interphase reported recently.

Interphase	**Cycling stability** (current density (mA cm^{-2})/capacity (mAh cm^{-2}) (life span (h))	E_a	Ref.
PDA-TMT-MesoCOF@Zn	**5-1 2700**	**17.85 KJ mol^{-1}**	**This work**
COF@Zn	1-1 2500	41.82 KJ mol^{-1}	22
Tp-Tg@Zn	5-1 1442	29.26 KJ mol^{-1}	23
G-COF@ Zn	3-1 1650	24.5 KJ mol^{-1}	24
PI-DT-COF@Zn	10-1 200	39.25 KJ mol^{-1}	25
Zn@COF-S-F	1.5-0.75 1000	/	26
PVC-Zn-AAN-COF@Zn	20-1 300	/	27
TpBD-2F@ Zn	2-2 1200	22.3 KJ mol^{-1}	28
Zn@iCOF-ED	1-1 >1000	/	29

Table S4. Benchmarking of the cycling stability of PDA-TMT-MesoCOF@Zn against state-of-the-art Zn anode protective layers in symmetric cells.

Interphase	Current Density (mA cm^{-2})	Capacity (mAh cm^{-2})	Life (h)	Reference
PDA-TMT-MesoCOF@Zn	**5**	1	2700	**This work**
VAA-Zn-TMA@Zn	5	1	2400	30
DEDBA-MCHD-Zn	5	5	1000	31
CUR@Zn	1	1	2000	32
ME-ZIF8	5	1	1900	33
BIL@Zn	5	1	1200	34
Zn@ZSiF	1	1	1800	35
COF@Zn	1	1	2500	22
ZIF-7/SA@Zn	1	1	1500	36
GCuCN@Zn	1	1	2000	37

REFERENCES

1. C. Yang, Y. Pan, H. Yu, X. Hu, X. Li and C. Deng, *Adv. Sci.*, 2023, **10**, 2302109.
2. Y. Y. Qian, Y. L. Han, X. Y. Zhang, G. Yang, G. Z. Zhang and H. L. Jiang, *Nat. Commun.*, 2023, **14**, 3083.
3. Y. Liu, H. Wu, L. Guo, W. Zhou, Z. Zhang, Q. Yang, Y. Yang, Q. Ren and Z. Bao, *Angew Chem Int Ed.*, 2022, **61**, e202117609.
4. G. Kresse and J. Furthmüller, *Comput. Mater. Sci*, 1996, **6**, 15-50.
5. J. P. Perdew, K. Burke and M. Ernzerhof, *Phys. Rev. Lett.*, 1996, **77**, 3865-3868.
6. S. Grimme, J. Antony, S. Ehrlich and H. Krieg, *J Chem Phys*, 2010, **132**, 154104.
7. B. Bao, Y. Hao, X. Wu, R. Xiao, C. Hou, Y. Li, Q. Zhang, K. Li and H. Wang, *Sci. Adv.*, **11**, eaea1304.
8. H. Yin, H. Huang, L. Bai, Z. Liu, X. Yan, R. Sun, Z. Li, F. Bai, E. Chen, L. Xiong, J. Tang and L. Jing, *Angew Chem Int Ed.*, 2025, **64**, e202505886.
9. J. Almarza, I. Cardillo-Zallo, K. Strutyński, M. Martínez-Abadía, N. M. Padial, C. Martí-Gastaldo, M. Melle-Franco, A. N. Khlobystov and A. Mateo-Alonso, *Angew. Chem. Int. Ed.*, 2025, **64**, e202505935.
10. H. Chen, G. Guo, W. Li, S. Ke, H. Zhang, J. Fu, C. Jing and S. Liu, *Angew. Chem. Int. Ed.*, 2026, **65**, e17356.
11. L. Huang, W. Li, F. Wei, S. Ke, H. Chen, C. Jing, J. Cheng and S. Liu, *Chem*, 2024, **10**, 3100-3113.
12. H. Wu, S. Yin, H. Zhang, H. Xu, Y. Luo, F. Li and D. Zhao, *J.Am.Chem.Soc.*, 2025, **147**, 21089-21096.
13. N. He, Y. Zou, C. Chen, M. Tan, Y. Zhang, X. Li, Z. Jia, J. Zhang, H. Long, H. Peng, K. Yu, B. Jiang, Z. Han, N. Liu, Y. Li and L. Ma, *Nat. Commun.*, 2024, **15**, 3896.
14. J. Hong, B. Zhu, M. Song, X. Wang, B. Gao, Y. Liu and X. Huang, *Adv. Funct. Mater.*, 2025, **35**, 2424731.
15. Z. Li, Q. Zhu, Y. Li, Y. Yang, Y. Ju, M. Xu and B. Xu, *Chin. Chem. Lett.*, 2025, 111348.
16. X. Li, F. Chen, Y. Ye, C. Wang, G. Ding, Y. Zhang, X. Xiao, L. Li, Z.-G. Guo, L.-C. Jia, J. Lei, G.-J. Zhong, H. Yang, S. Zhou and Z.-M. Li, *Small*, 2025, **21**, 2501855.
17. S. Zhang, C. Liu, Y. Wang, A. Xu, C. Chen and X. Liu, *Chem. Sci.*, 2025, **16**, 5651-5661.
18. M. Tabish, Y. Chen, A. Kumar, M. Mubeen, Z. Jiang, N. Muhammad, L. Guo, X. Chen, J. Zhao, G. Yasin, L. Qin and H. Song, *Small*, 2025, **21**, 2505802.
19. P. X. Sun, Y. Q. Zheng, X. Y. Zhang, H. Yu, Y. Guo and L. Yu, *Adv. Energy Mater.*, 2024, **14**, 2304138.
20. T.-B. Song, Q.-L. Ma, X.-R. Zhang, J.-W. Ni, T.-L. He and H.-M. Xiong, *Chem. Eng. J.*, 2023, **471**, 144735.
21. Z. Miao, F. Zhang, H. Zhao, M. Du, H. Li, H. Jiang, W. Li, Y. Sang, H. Liu and S. Wang, *Adv. Funct. Mater.*, 2022, **32**, 2111635.
22. X. J. Y.Wang, W.Liang, et al. , *Adv. Mater.*, 2025, **37**, 2503086.
23. Y. Zou, Y. Mu, T. Wang, Z. Chen, Z. Shi, W. Guo, T. Shen, Z. Meng, J. Hu, L. Zeng, T. Liu and J. Sun, *Angew. Chem. Int. Ed.*, 2025, **64**, e202510080.
24. P. He, B. Li, B. Wang, D. Xie, K. Wang and W. Ai, *ACS Appl. Mater. Interfaces.*, 2025, **17**, 2556-2565.
25. C. Guo, X. Huang, J. Huang, X. Tian, Y. Chen, W. Feng, J. Zhou, Q. Li, Y. Chen, S.-L. Li and

Y.-Q. Lan, *Angew. Chem. Int. Ed.*, 2024, **63**, e202403918.
26. B. Li, P. Ruan, X. Xu, Z. He, X. Zhu, L. Pan, Z. Peng, Y. Liu, P. Zhou, B. Lu, L. Dai and J. Zhou, *Nano-Micro Lett.*, 2024, **16**, 76.
27. C. Guo, J. Zhou, Y. Chen, H. Zhuang, Q. Li, J. Li, X. Tian, Y. Zhang, X. Yao, Y. Chen, S.-L. Li and Y.-Q. Lan, *Angew. Chem. Int. Ed.*, 2022, **134**, e202210871.
28. D. Lei, W. Shang, L. Cheng, Poonam, W. Kaiser, P. Banerjee, S. Tu, O. Henrotte, J. Zhang, A. Gagliardi, J. Jinschek, E. Cortés, P. Müller-Buschbaum, A. S. Bandarenka, M. Z. Hussain and R. A. Fischer, *Adv. Energy Mater.*, 2024, **14**, 2403030.
29. L. Yang, Q. Ma, Y. Yin, D. Luo, Y. Shen, H. Dou, N. Zhu, R. Feng, Y. Kong, A. Yu, B. Cheng, X. Wang and Z. Chen, *Nano Energ.*, 2023, **117**, 108799.
30. Z. Li, G. Zhao, X. Chu, L. Sun, T. Jiang, R. Luo, Z. Zhang, Z. Cheng, Y. Qiu, M. Chen and W. Chen, *Angew. Chem. Int. Ed.*, 2026, **65**, e19208.
31. Y. Hu, L. Chen, W. Ding, Y. Wu, B. Tian, C. Yang and Y. Wang, *Adv. Mater.*, 2026, **38**, e21198.
32. M. Tang, Q. Liu, G. Liu, X. Zou, K. Zhang, Z. Yu, B. Zhang and L. An, *Nano-Micro Lett.*, 2026, **18**, 121.
33. X. Li, J. Chen, T. Wang, B. Wang, Y. Cao, D. Chao and Y. Tang, *Angew. Chem. Int. Ed.*, 2025, **64**, e202505855.
34. Z. Guo, Z. Liu, Y. Zhang, H. Li, M. Qi, C. Zhao, X. Zhang, Z. Wu, J. Yuan and N. Zhang, *Matter*, 2025, **8**, 102269.
35. G.-Y. Yin, H.-R. Wang, M.-Y. Zhou, T. Long, M.-S. Ding, B. Xie, X.-W. Wu, J. Li, W. Ling, J. Dai and X.-X. Zeng, *Angew. Chem. Int. Ed.*, 2025, **64**, e202423244.
36. G. Wu, W. Yang, Y. Yang, Y.-K. Choe and E. Yoo, *ACS Nano*, 2025, **19**, 18244-18255.
37. W. Zhang, Q. Yao, C. Wang, R. Feng, N. Chen, J. Zhu and Z. Li, *Adv. Funct. Mater.*, 2024, **34**, 2303590.